Journal of Materials Chemistry A

Surface energy-driven ex-situ hierarchical assembly of low-dimensional nanomaterials on graphene aerogels: A versatile strategy

Journal:	*Journal of Materials Chemistry A*
Manuscript ID	TA-ART-07-2018-007338.R1
Article Type:	Paper
Date Submitted by the Author:	06-Sep-2018
Complete List of Authors:	Pan, Long; ETH Zürich, Department of Materials Gao, Peiyuan; Pacific Northwest National Laboratory Tervoort, Elena; ETH-Zurich, Department of Materials Tartakovsky, Alexandre; Pacific Northwest National Laboratory Niederberger, Markus; ETH Zurich, Department of Materials

Journal Name

ARTICLE

Surface energy-driven *ex-situ* hierarchical assembly of low-dimensional nanomaterials on graphene aerogels: A versatile strategy

Received 00th January 20xx,
Accepted 00th January 20xx

DOI: 10.1039/x0xx00000x

www.rsc.org/

Long Pan,‡[a,*] Peiyuan Gao,‡[b] Elena Tervoort,[a] Alexandre M. Tartakovsky[b] and Markus Niederberger[a,*]

Hybrid aerogels composed of functional low-dimensional nanomaterials (LDNs) and reduced graphene oxide (rGO) hold great promise in the fields ranging from catalysis to energy storage and conversion. However, the challenge of developing a general strategy for the hierarchical assembly of LDNs on rGO aerogels remains unsolved. Here, we propose a surface energy-driven strategy for *ex-situ* hierarchical assembly of LDNs on preformed rGO aerogels. This strategy is versatile and generally applicable to a broad variety of LDNs regardless of their composition, shapes, and dimensionalities. Experimental and simulation results reveal that the organically modified, energetically stable LDNs thermodynamically tend to uniformly and densely reside on the rGO aerogels, thereby reducing the surface energy of the aerogels and the free energy of the solution system. Four kinds of LDNs are successfully decorated on rGO aerogels, including 0D Mn_3O_4 nanocubes and Ag nanospheres, and 1D TiO_2 nanochains and SnO_2 nanowires. As a possible application harnessing the unique structural features of these materials, the Mn_3O_4@rGO hybrid aerogels were tested as anodes in lithium ion battery half cells, delivering a high reversible lithium storage capacity (1.35 mA h cm^{-2} at 3.5 mA cm^{-2}) at high mass loading density (up to 7 $mgcm^{-2}$).

Introduction

Aerogels are solid materials composed of a three-dimensional (3D), interconnected network with open-celled pores that are filled with air.[1] The porous structure of aerogels endows them with high specific surface areas, large pore volumes, and extremely low density, making them attractive for applications in, e.g., energy storage and conversion, catalysis, and sensing.[2] Aerogels are typically composed of low dimensional nanomaterials (LDNs), including 0D nanoparticles, 1D nanotubes/nanowires/nanochains, or 2D nanosheets.[3] They may consist of just one type of building block as in the case of single component aerogels or they combine several different ones, resulting in hybrid or composite aerogels. Classical sol-gel routes generally produce single component aerogels with silica representing the most studied composition. But single component aerogels suffer from limited functionality due to the compositional simplicity and from low mechanical strength, which makes the materials extremely brittle. In hybrid or composite aerogels these limitations can largely be overcome. Multicomponent aerogels do not only provide the characteristic porous structure and the low density of aerogels, but also exhibit integrated functionalities and synergistic effects as a result of the different building blocks and their interactions.[4]

Graphene, a typical 2D material, exhibits many exceptional properties, such as high conductivity (6000 S cm^{-1}), large specific surface area (2630 m^2 g^{-1}), and good mechanical strength (130 GPa).[5] Given the difficulty of directly handling graphene, reduced graphene oxide (rGO) is used far more often in both scientific and industrial research. rGO can be produced in large quantities, can easily be processed in liquid medium and its properties come close to those of graphene. These unique features make rGO the ideal substrate for hybridization with other LDNs, greatly contributing to the increase in electronic conductivity and to the reduction of the mechanical deficiencies of LDN based aerogels.[6] Besides, rGO itself can be assembled into aerogels with high mechanical strength and excellent electrical and thermal conductivity,[7] thus serving as a tough framework to support those LDNs that are not easy to process into stable aerogels, such as metal nanoparticles.[8] Therefore, rGO is highlighted not only as an efficient additive to improve the conductivity, but also as a robust scaffold to enhance the mechanical strength of LDNs aerogels.

For the preparation of LDNs@rGO hybrid aerogels, the *in-situ* hydrothermal reaction is most frequently used, through which graphene oxide (GO) is reduced to rGO and at the same

[a] *Laboratory for Multifunctional Materials, Department of Materials, ETH Zurich, Vladimir-Prelog-Weg 5, 8093, Zurich, Switzerland. *Email: long.pan@mat.ethz.ch, markus.niederberger@mat.ethz.ch*

[b] *Advanced Computing, Mathematics, and Data Division, Pacific Northwest National Laboratory, Richland, Washington, 99352, United States.*

† Electronic Supplementary Information (ESI) available: Supplementary ▮▮igures and tables. See DOI: 10.1039/x0xx00000x

‡ These authors contributed equally to this work.

time the LDNs are directly grown from the molecular precursors on the rGO nanosheets.[9] With this method, a great variety of LDNs such as 0D nanoparticles and 1D nanorods/nanowires have been assembled on rGO aerogels.[10] However, it is not a general approach for decorating LDNs on rGO aerogels. First, the morphology and the composition of the resulting LDNs cannot be precisely predicted before the hydrothermal reactions, which makes it difficult to obtain a hybrid aerogel with a specific architecture. Second, each kind of hybrid aerogel needs a unique set of reaction conditions during the hydrothermal treatment, limiting the compositional variety. Last but not the least, the hydrothermal reaction is more like a "black box", which means that the mechanism for the assembly of LDNs on rGO aerogels is unknown. In this sense, it remains challenging to develop a rational and predictable approach to assemble compositionally, structurally and morphologically defined LDNs on rGO aerogels. Such an extensive control over the building blocks as well as on their assembly is a prerequisite to optimize the properties of aerogels for specific applications.

Differing from the *in-situ* hydrothermal synthesis, the *ex-situ* assembly route starts from performed, well-defined LDNs, providing the basis for maximum control over the LDNs@rGO hybrid aerogel synthesis. Herein we propose a surface energy-driven strategy for *ex-situ* hierarchical assembly of LDNs on rGO aerogels, which is applicable to many different LDNs regardless of their composition, shapes, and dimensionalities. To underline the high versatility of the approach, four kinds of LDNs, i.e., 0D Mn_3O_4 nanocubes, 0D Ag nanospheres, 1D TiO_2 nanochains, and 1D SnO_2 nanowires, are successfully assembled on rGO aerogels in a homogeneous and dense way. The surface energy provides the thermodynamic driving force for the LDNs to bind to the rGO aerogels, which is confirmed by experimental and simulation results. The resulting LNDs@rGO hybrid aerogels effectively integrate the functionalities of the two building blocks. As a proof-of-concept application taking advantage of the unique features of these materials, the Mn_3O_4@rGO hybrid aerogels were tested

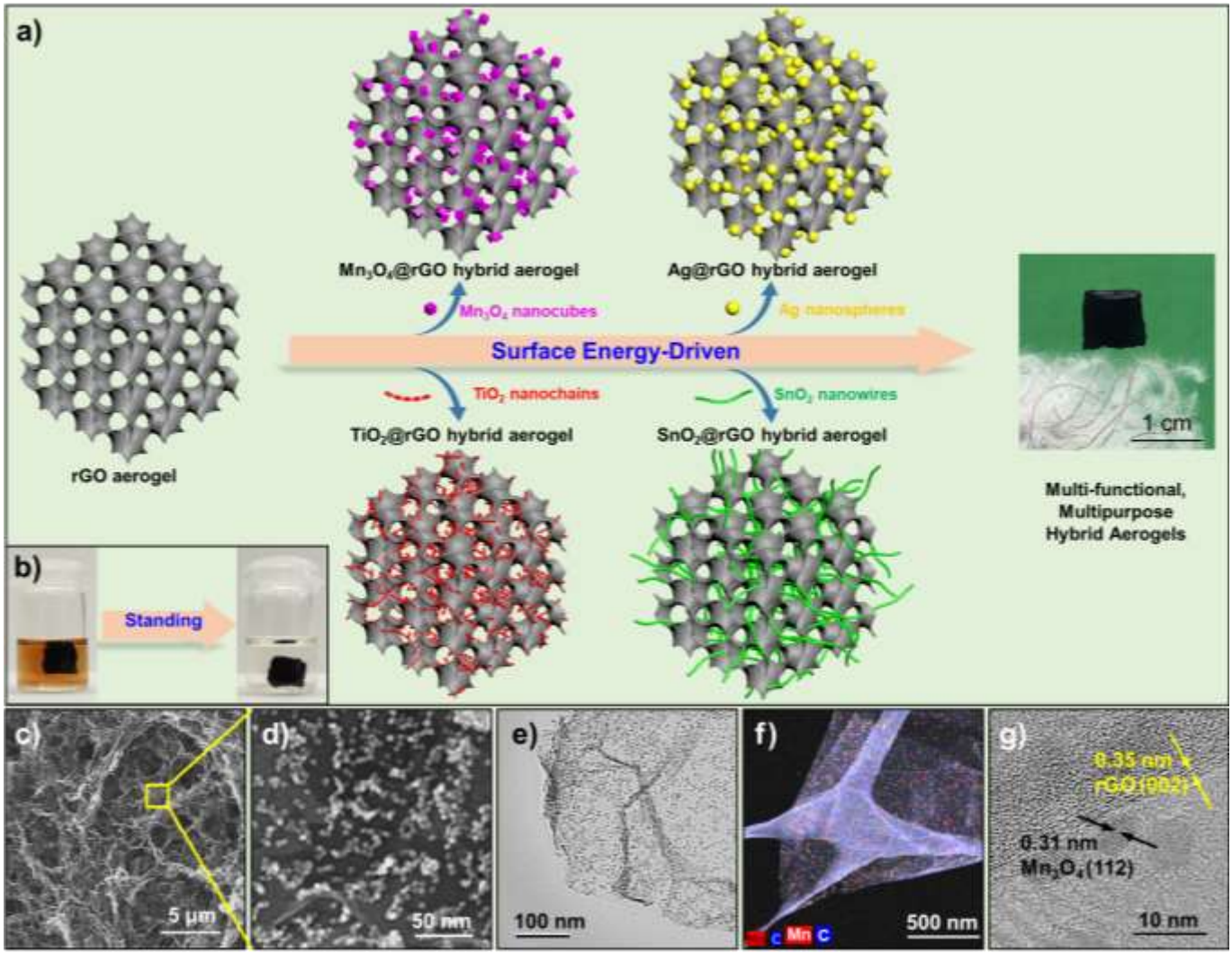

Fig. 1 (a) Schematic illustration of the surface energy-driven *ex-situ* hierarchical assembly of LDNs on rGO aerogels; (b) photographs of an rGO aerogel monolith in Mn_3O_4/THF dispersion before and after assembly; (c) low- and (d) high-magnification SEM images, (e) TEM image, (f) STEM image with EDS mappings, and (g) HRTEM image of a Mn_3O_4@rGO hybrid aerogel. The inset in (a) shows a low density Mn_3O_4@rGO hybrid aerogel standing on an ultralight Clematis Virgin's Bower seed.

as anodes in lithium ion battery half cells, delivering an impressive lithium storage performance (1.35 mA h cm^{-2} at 3.5 mA cm^{-2}) at high mass loading density (up to 7 mg cm^{-2}).

Results and discussion

Fig. 1a illustrates the process of surface energy-driven *ex-situ* hierarchical assembly of LDNs on rGO aerogels. In the first step, the two building blocks, i.e., the rGO aerogel and the LDNs (e.g., 0D Mn_3O_4 nanocubes, 0D Ag nanospheres, 1D TiO_2 nanochains, and 1D SnO_2 nanowires) are synthesized separately. The detailed characterization of the rGO aerogels and LDNs are presented in **Fig. S1–S11**. rGO aerogels composed of rGO nanosheets have a large surface energy in poor solvents, such as tetrahydrofuran (THF), hexane, and methanol, due to the unmatched Hansen solubility parameters.[11] In contrast, the organically modified LDNs are energetically stable in such solvents (insets of **Fig. S2–S5**). Once the LDNs are combined with rGO aerogels, they are thermodynamically driven to reside on the rGO nanosheets, thereby reducing the surface energy of rGO aerogels and the total free energy of the solution system.[12] The surface energy-driven mechanism for the hierarchical assembly of LDNs on rGO aerogels is further proved by experiments and simulation, as discussed later. After supercritical drying, low-density LDNs@rGO hybrid aerogels, e.g., Mn_3O_4@rGO, Ag@rGO, TiO_2@rGO, and SnO_2@rGO, are obtained. This strategy seems to be broadly applicable to many different LDNs and thus may open up a general pathway for the construction of a broad variety of advanced LDNs@rGO hybrid aerogels.

Fig. 1b presents a digital photograph of the experimental setup for the surface energy-driven strategy, in which a rGO aerogel monolith is mixed with a Mn_3O_4/THF dispersion (yellowish-brown). After standing over three weeks, the dispersion becomes nearly transparent, indicating the successful and highly efficient adsorption of Mn_3O_4 nanocubes on the rGO aerogel. The monolithic shape underlines the good mechanical strength of the resulting Mn_3O_4@rGO aerogel, which is crucial for many applications. **Fig. 1c–g** display the typical morphology of the Mn_3O_4@rGO aerogels. According to scanning electron microscopy (SEM) image (**Fig. 1c**), the porous structure of the rGO aerogel including low density, high specific surface area and extensive micro- and mesoporosity is fully preserved in the composite material. At higher magnification (**Fig. 1d**) it can be clearly seen that the Mn_3O_4 nanocubes are uniformly and densely arranged on the rGO aerogel, which is also confirmed by the transmission electron microscopy (TEM) image (**Fig. 1e**). To further disclose the uniform assembly of Mn_3O_4 nanocubes on the rGO nanosheets, high-angle annular dark-field (HADDF) scanning TEM (STEM) combined with energy dispersive X-ray spectroscopy (EDS) is employed, as shown in **Fig. 1f**. The elemental maps of Mn and C agree well with the corresponding STEM image, firmly demonstrating the presence and homogeneous distribution of Mn_3O_4 nanocubes throughout the whole rGO surface. Besides, the co-existence

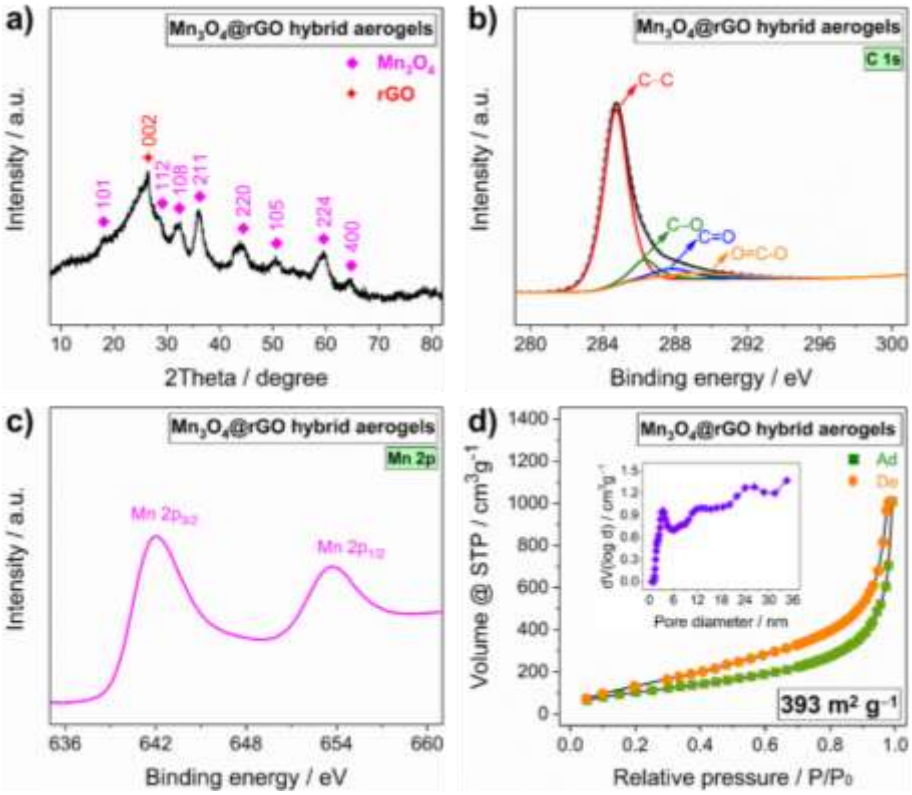

Fig. 2 (a) XRD pattern, (b) C 1s and (c) Mn 2p XPS spectra, and (d) N_2 adsorption-desorption isotherms of Mn_3O_4@rGO hybrid aerogels.

of (002) plane of rGO and (112) plane of Mn_3O_4 in the high-resolution TEM (HRTEM) image (**Fig. 1g**) confirms the successful assembly of Mn_3O_4 nanocubes on the basal planes of rGO nanosheets.[13] **Fig. S12** shows typical thermogravimetric analysis (TGA) curves of Mn_3O_4 nanocubes, rGO aerogels, and Mn_3O_4@rGO hybrid aerogels. The content of Mn_3O_4 nanocubes in the Mn_3O_4@rGO hybrid aerogel is 58 wt%, which is in good agreement with their initial amount of 60 wt% (**Table S1**). Obviously, the adsorption efficiency is very high, resulting in the incorporation of all Mn_3O_4 nanocubes in the dispersion into the aerogel scaffold.

X-ray diffraction (XRD) is performed to investigate the crystallinity and to gain phase information for the resulting hybrid aerogels. As seen from the XRD pattern of the Mn_3O_4@rGO hybrid aerogel (**Fig. 2a**), the intensive peak at 26.4° is attributed to the (002) reflection of few-layer rGO,[7c] and the calculated lattice spacing of 0.34 nm is in accordance with the value observed in HRTEM (**Fig. 1g**). Besides, the (101), (112), (108), (211), (220), (105), (224), and (400) reflections can be indexed to the spinel Mn_3O_4.[14] X-ray photoelectron spectroscopy (XPS) is employed to reveal the chemical state of the resulting hybrid aerogels. Strong peaks corresponding to C, O and Mn can be readily recognized in the survey spectrum (**Fig. S13**), confirming once more the co-existence of Mn_3O_4 and rGO. To figure out the chemical nature, high-resolution C 1s and Mn 2p XPS spectra are provided in **Fig. 2b** and **2c**. In the C1s spectrum the most prominent peak at 284.7 eV corresponds to the C–C bonds, and three minor peaks at 286.3, 287.8, and 289.2 eV are attributed to the C–O, C=O, and O=C–O bonds, respectively.[7a] The C1s chemical state remains the same in both the rGO and in the Mn_3O_4@rGO aerogel (**Fig. S6**). Together with the Raman results (**Fig. S14**), the unaltered C1s chemical state indicates that only very few, if any at all, new defects and chemical bonds are formed during the hierarchical assembly process, which means that the surface energy-driven strategy is nondestructive to the building blocks. The Mn 2p spectrum presents two well-resolved, strong peaks located at 641.9 and 653.7 eV, corresponding to the Mn 2p3/2 and 2p1/2 orbitals of spinel Mn_3O_4,[13] which is in good agreement with the XRD results. Brunauer–Emmett–Teller (BET) analysis is used to uncover the porous nature of the resulting hybrid aerogels. Even with the relatively heavy Mn_3O_4 nanocubes, the Mn_3O_4@rGO hybrid aerogels still have a large surface area (393 m^2 g^{-1}) as well as considerable micro- and mesoporosity (pore volume = 1.6 cm^3 g^{-1}), as shown in **Fig. 2d**.

The surface energy-driven assembly mechanism is

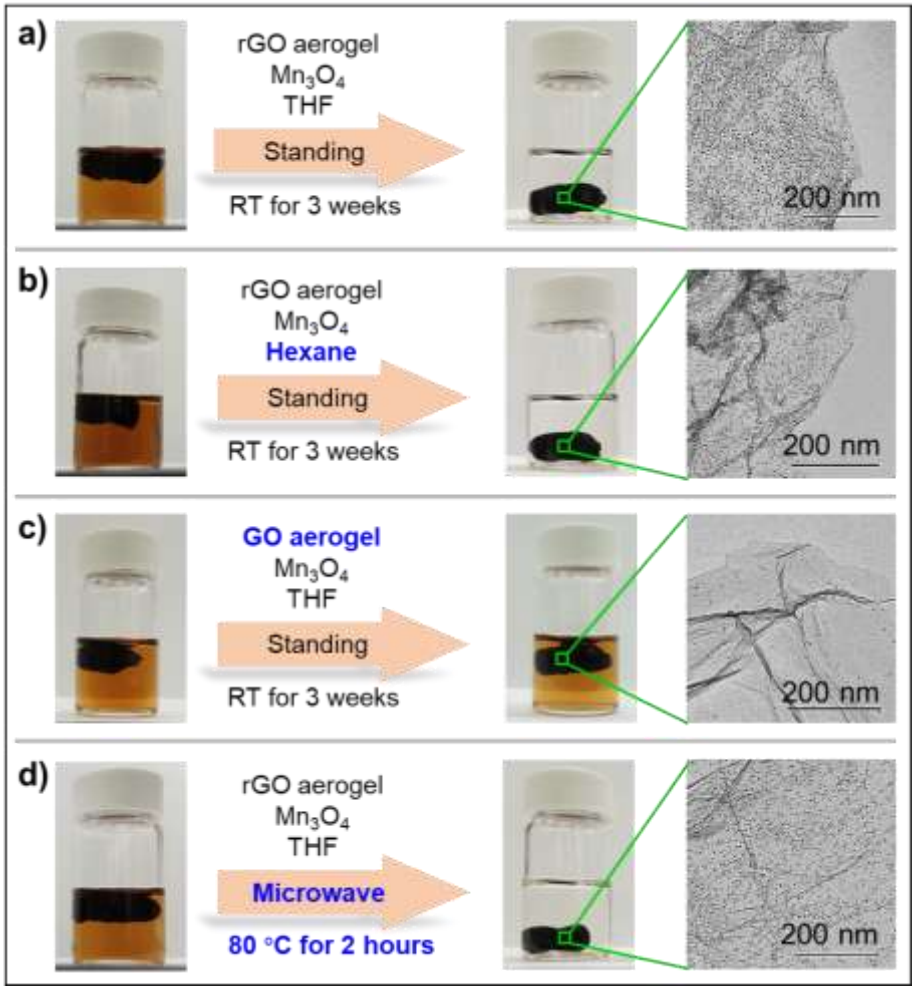

Fig. 3 Digital photographs of the assembly process under different experimental conditions and corresponding TEM images of the resulting Mn_3O_4@rGO hybrid aerogels.

addressed from an experimental as well as from a simulation point of view. **Fig. 3** presents photographs and TEM images of Mn_3O_4@rGO hybrid aerogels obtained under different experimental conditions. The parameter, which was changed in a specific experiment, is highlighted in blue in **Fig. 3** and includes solvent, the carbon aerogel network and the assembly technique. As stated above, THF and hexane are poor solvents for the rGO nanosheets, in which the high surface energy of the rGO nanosheets cannot be compensated.[11] Once the solvated, organically modified and stable Mn_3O_4 nanocubes are introduced, surface energy minimization drives them to spontaneously assemble on the rGO nanosheet-based aerogels, as shown in **Fig. 3a** (THF) and **3b** (hexane). In contrast, in a good solvent (e.g., *N*-methyl pyrrolidone) the rGO nanosheets have a minimized surface energy due to the matched Hansen solubility parameters,[11] therefore the nanoparticles do not attach to them without outside linkers, which has been extensively investigated before.[15] Apart of using different solvents, also graphene oxide (GO) aerogels are used as host for the Mn_3O_4 nanocubes to confirm the surface energy-driven mechanism. In contrast to rGO, GO can be well solvated and thus has a relatively low surface energy in THF due to the presence of significant amount of oxygen functional groups.[16] As expected, only few Mn_3O_4 nanocubes are assembled on GO aerogels, which is verified by the slight color change of Mn_3O_4/THF dispersion and by the TEM image (**Fig. 3c**). These results confirm that surface energy is the driving force for the hierarchical assembly of Mn_3O_4 nanocubes on the rGO aerogels. Interestingly, it is found that microwave irradiation can significantly speed up the assembly process, reducing the reaction time from three weeks to 2 hours at 80 °C (**Fig. 3d**). This effect may be mainly attributed to the dielectric heating characteristic of microwave irradiation, rather than to the faster Brownian motion (**Fig. S15**).[17] The morphology of the resulting Mn_3O_4@rGO hybrid aerogels remains unchanged, which, together with the short assembly time, may help to scale up the production of LDNs@rGO hybrid aerogels.

To better understand the surface energy-driven assembly mechanism, several all-atom molecular dynamics (MD) simulations of graphene nanosheets, oleylamine (OA) molecules, and OA-modified Mn_3O_4 nanocubes in THF are performed. Since the rGO is reduced and the sp^2-hybridized carbon network is highly recovered, we use defect-free graphene as an ideal model in the simulation. **Fig. S16** displays the final state of two individual graphene nanosheets dispersed in THF. They are not stable and restack into multilayered structures. In **Fig. 4a,** we show that OA molecules bind to the graphene nanosheets in THF, rendering them dispersible in THF without agglomeration or restacking. **Fig. 4b** and **4c** show the initial and final configuration of simulations for the OA-modified Mn_3O_4/graphene/THF system, respectively. The OA molecules on the Mn_3O_4 nanocubes facing towards the graphene nanosheets are attached to them by hydrophobic interactions,[11a] while all the other OA chains around the nanocubes form micelle-like entities.[11d] Therefore, the OA-modified Mn_3O_4 nanocubes behave as surfactants, absorbing on the graphene surface, and thermodynamically stabilizing the graphene. **Fig. 4d** presents the order parameter of the OA backbone (see the definition in *Experimental*) along the direction perpendicular to the graphene nanosheet. The value is -0.25 in the layer close to the graphene surface, indicating that the OA molecules or parts of the OA molecules in this layer are oriented parallel to the surface. More interesting, the principal axis of the Mn_3O_4 nanocubes in the simulation is not parallel to the graphene.

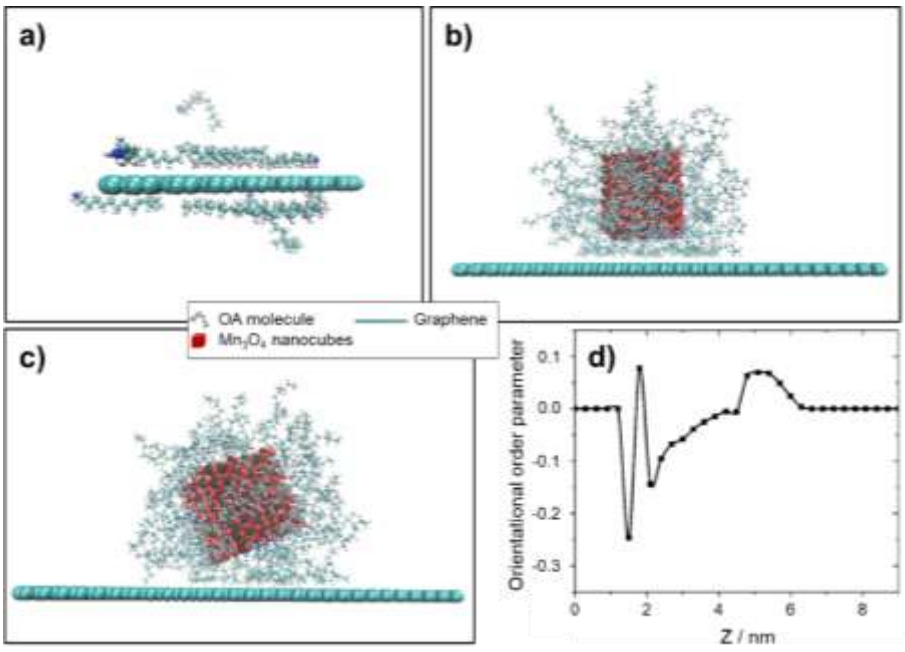

Fig. 4 All-atom MD simulation. (a) Final state of OA molecules and graphene in THF; (b) initial and (c) final state of OA modified Mn_3O_4 nanocubes and graphene in THF; (d) the order parameter of OA molecules along the direction perpendicular to graphene nanosheets. For clarity the THF molecules are not shown.

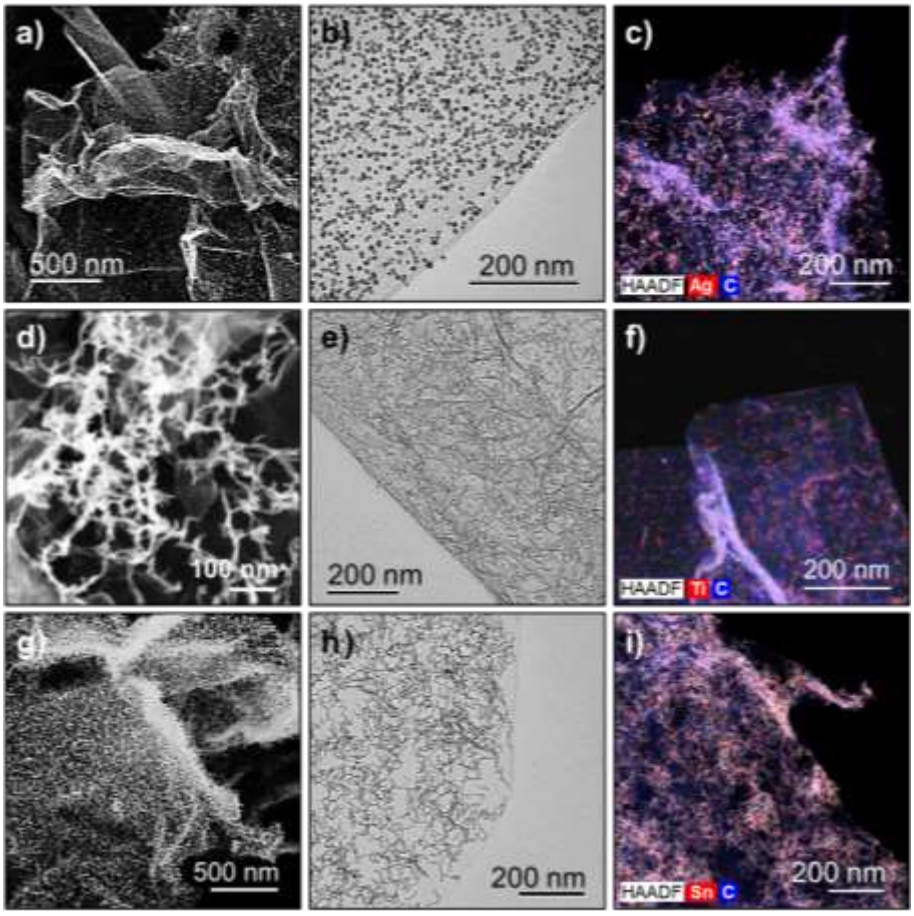

Fig. 5 (a-c) Ag@rGO, (d-f) TiO_2@rGO, and (g-i) SnO_2@rGO hybrid aerogels: (a, d, g) SEM images, (b, e, h) TEM images, and (c, f, i) STEM images with EDS mappings.

The reason is that in the simulation the length of the OA molecules is a bit longer than the sides of the Mn_3O_4 nanocubes. To reduce the surface energy, more OA molecules tend to be absorbed on graphene. The skewed configuration of the Mn_3O_4 nanocubes allows more OA molecules on other facets of the Mn_3O_4 nanocubes to be in contact with the graphene, which further indicates that the effect of the OA-modified Mn_3O_4 nanocubes is similar to surfactants. In the experiment, the Mn_3O_4 nanocubes are much larger than in our simulation. Therefore, it is expected that in reality the principal axis of the Mn_3O_4 nanocubes will be parallel to graphene to maximize the number of OA molecules in contact with the graphene. Owing to the hydrophobic nature of graphene, their noncovalent functionalization with surfactants is an effective method to reduce the surface energy of graphene in THF. In contrast to regular surfactants, the size of Mn_3O_4 nanocubes is also an important factor for the dispersion of graphene since they have large excluded volume (**Fig. S17**).

The surface energy-driven hierarchical assembly strategy is applicable to many different LDNs regardless of their composition (metal or metal oxide), shapes (nanocubes or nanospheres), or dimensionalities (0D or 1D). In this sense, other three LDNs, i.e., 0D Ag nanospheres, 1D TiO_2 nanochains, and 1D SnO_2 nanowires, are employed to demonstrate the versatility of this strategy. **Fig. 5** presents the morphologies of the resulting Ag@rGO, TiO_2@rGO and SnO_2@rGO hybrid aerogels. As disclosed by the SEM images (**Fig. 5a**, **5d**, and **5g**), the porous structure of rGO aerogels is well preserved in these three composite aerogels, similar to the Mn_3O_4@rGO hybrid aerogel. The three LDNs are also successfully assembled on preformed rGO aerogels in a uniform and dense way, which is further verified by the TEM results (**Fig. 5b**, **5e**, and **5h**) and EDS mappings (**Fig. 5c**, **5f**, and **5i**). These results indicate that the surface energy-driven assembly is not at all limited to 0D nanoparticles, but can be extended to much larger 1D nanochains and nanowires. Apart from the microstructures, also the crystallinity and crystal phase of the Ag@rGO, TiO_2@rGO, and SnO_2@rGO aerogels are characterized by XRD and HRTEM (**Fig. S18**). In all cases, the initial morphological and structural features of the rGO aerogels and the LDNs are fully preserved, confirming once more that the surface energy-driven hierarchical assembly process is nondestructive to the building blocks.

Combining the properties of the two building blocks with high porosity and low density, LDNs@rGO hybrid aerogels hold great promise in energy storage devices. Lithium-ion batteries (LIBs), the most popular energy storage means for portable electronics and electric vehicles, are demanding high capacity, especially areal capacity.[18] Although LDNs@rGO nanocomposites can deliver high gravimetric capacities, the mass loading density is rather low (< 2 mg cm^{-2}),[19] thereby leading to relatively low areal capacities. Besides, the

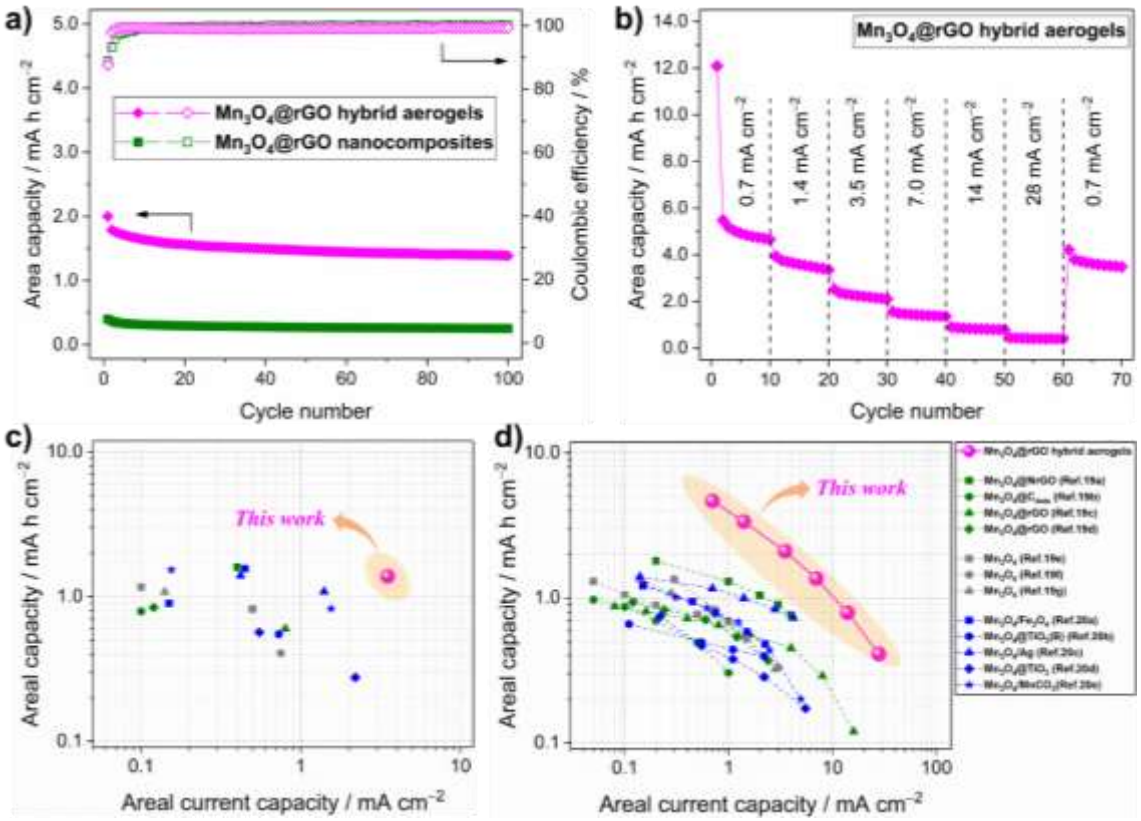

Fig. 6 (a) Cycling behavior of Mn_3O_4@rGO hybrid aerogels and Mn_3O_4@rGO nanocomposites at a mass loading density of 7 mg cm^{-2} (current density = 3.5 mA cm^{-2}); (b) rate capability of Mn_3O_4@rGO hybrid aerogels; comparison of (c) reversible capacities and (d) rate capabilities of Mn_3O_4@rGO hybrid aerogels with other representative Mn_3O_4 based anode materials reported recently.

gravimetric capacity decreases dramatically as the mass loading density increases, which severely compromises the practical application of LDNs@rGO nanocomposites. Mn_3O_4 is a promising anode material for LIBs due to its high theoretical capacity (937 mA h g^{-1}), low cost, and low toxicity.[19] Here we demonstrate that the Mn_3O_4@rGO hybrid aerogels can deliver much better lithium storage performance than the powdery Mn_3O_4@rGO nanocomposites (see *Experimental Details*) even at high mass loading density (up to 7 mg cm^{-2}), as shown in **Fig. 6**. As expected, the Mn_3O_4@rGO nanocomposites deliver a reversible areal capacity of only 0.25 mA h cm^{-2} at an areal current density of 3.5 mA cm^{-2} after 100 cycles. This largely irreversible capacity loss is mainly ascribed to the increasing ion diffusion pathways in thicker electrodes (higher mass loading density), as illustrated in **Fig. S19a**.[18a] For the Mn_3O_4@rGO hybrid aerogels, the porous structure endows them with large surface areas for numerous active sites in contact with the electrolyte as well as interconnected channels for fast diffusion of Li^+ ions (**Fig. S19b**).[18a] As a result, Mn_3O_4@rGO hybrid aerogels deliver an impressive reversible areal capacity of 1.38 mA h cm^{-2} at an areal current density of 3.5 mA cm^{-2} after 100 cycles, which is 452% higher than that of the Mn_3O_4@rGO nanocomposites. Besides, the areal capacity of Mn_3O_4@rGO hybrid aerogels is much higher than that of pure rGO aerogels and pure Mn_3O_4 nanocubes (**Fig. S20**), indicating the significant synergy between rGO aerogels and Mn_3O_4 nanocubes. The excellent rate capabilities of the Mn_3O_4@rGO hybrid aerogels are presented in **Fig. 6b**. Reversible areal capacities of 4.66, 3.36, 2.10, 1.36, 0.79, and 0.41 mA h cm^{-2} are achieved at areal current densities of 0.7, 1.4, 3.5, 7.0, 14, and 28 mA cm^{-2}. Moreover, the capacity recovers immediately to 3.49 mA h cm^{-2} when the current density goes back to 0.7 mA cm^{-2}. The lithium storage kinetics of the Mn_3O_4@rGO hybrid aerogels is also investigated by CV measurement at different sweep rate, as shown in **Fig. S21**. The capacitive contribution to the total capacity is about 39.1 % at a relatively high sweep rate (1 mV s^{-1}). This moderately high capacitive contribution is caused by the high surface area of the hybrid aerogel and the small size of the Mn_3O_4 nanocubes. Compared to other representative Mn_3O_4 based anode materials reported recently (**Fig. 6c** and **6d**),[19,20] our Mn_3O_4@rGO hybrid aerogels show superior lithium storage performance in both reversible areal capacity and rate capabilities.

Conclusions

In summary, we introduced a surface energy-driven strategy for *ex-situ* hierarchical assembly of LDNs on rGO aerogels from preformed building blocks. The versatility of the approach was not only demonstrated experimentally, but the results were also supported and explained by simulation. The strategy works for a broad variety of LDNs regardless of their

composition, shapes, and dimensionalities. Four kinds of representative LDNs were successfully assembled on rGO aerogels in a uniform and dense way, including 0D Mn_3O_4 nanocubes, 0D Ag nanospheres, 1D TiO_2 nanochains, and 1D SnO_2 nanowires. The possibility of fabricating LDNs@rGO hybrid aerogels from different building blocks gives access to a broad range of functionalities, which can be combined with the specific structural features of aerogels such as high porosity and low density. As a proof-of-concept application, the Mn_3O_4@rGO hybrid aerogels were found to be promising anode materials for LIBs owing to their impressive lithium storage capabilities (1.38 mA h cm^{-2}@3.5 mA cm^{-2}) at high mass loading density (up to 7 mg cm^{-2}). The surface energy-driven strategy may open the door to the scalable and straightforward construction of advanced LDNs@rGO hybrid aerogels for applications, where high surface areas, connected porosity and structural flexibility are essential requirements.

Experimental

Synthesis of rGO Aerogels:[7a] Briefly, 20 μL of ethylenediamine (EDA) was added to 5 mL of GO suspension (3 mg mL^{-1}) , followed by heating in an oven at 95 °C for 6 h. After cooling down, GO hydrogels were obtained. The GO hydrogels were soaked in large amount of acetone for complete solvent exchange, dried by supercritical CO_2 and further annealed at 600 °C for 2 h under Ar atmosphere to obtain the rGO aerogels.

Synthesis of Mn_3O_4 Nanocubes:[14] Typically, 2 mmol of anhydrous manganese(II) acetate, 4 mmol of oleic acid and 20 mmol of oleylamine were dissolved in 30 mL of xylene and stirred at room temperature for 10 min. After heating to 90 °C, 2 mL of deionized water was injected and the solution was kept at 90 °C for another 2 h. The resulting Mn_3O_4 nanocubes were washed with ethanol several times and vacuum-dried at 80 °C overnight.

Synthesis of TiO_2 Nanochains:[21] In a typical experiment, 0.38 mmol of 2-amino-2-(hydroxymethyl)-1,3-propanediol (Trizma) was mixed with 10 mL of anhydrous benzyl alcohol. Then, 4.55 mmol of $TiCl_4$ was slowly added into the mixture under stirring. The solution was heated to 80 °C and aged for 24 h. The resulting TiO_2 nanochains were obtained by washing three times with acetone and vacuum-drying at 60 °C overnight.

Synthesis of Ag nanospheres:[12a] 10 mL of octadecylamine was heated to 180 °C. Then, 3 mmol of $AgNO_3$ were added, and the solution was kept at 180 °C for 25 min. After reaction, the upper suspension was discarded and the precipitate at the bottom was collected. The Ag nanoparticles were obtained by washing the precipitate with ethanol several times and vacuum-drying overnight.

Synthesis of SnO_2 Nanowires:[12b] Briefly, 5 mmol of tin (IV) chloride pentahydrate, 40 mmol of oleylamine, 10 mmol of oleic acid and 100 mmol of absolute ethanol were mixed in a 50 mL beaker. After stirring at room temperature for 10 min, the beaker with the solution was transferred to a 200 mL Teflon cup containing 20 mL of ethanol/water mixture(96/4 vol%). Then, the Teflon cup was sealed in a stainless steel autoclave and heated to 180 °C and kept for 18 h. The obtained SnO_2 nanowires were washed with ethanol several times and vaccum-dried overnight.

Hierarchical Assembly of LDNs on rGO Aerogels: In a typical experiment, LDNs, e.g., Mn_3O_4 nanocubes, Ag nanospheres, TiO_2 nanochains, and SnO_2 nanowires, were dispersed in THF, hexane or methanol. Then, rGO aerogels were soaked in the dispersion and kept at room temperature for more than 3 weeks. During this time, the LDNs were spontaneously assembled on the rGO aerogel driven by surface energy. After assembly, the resulting hybrid aerogels (Mn_3O_4@rGO, Ag@rGO, TiO_2@rGO, and SnO_2@rGO) were obtained by supercritical drying.

Synthesis of powdery Mn_3O_4@rGO nanocomposites: Mn_3O_4 nanocubes and rGO nanosheets were mixed at a ratio of 60/40 (wt%) in THF, followed by sonicating at an ultrasonic cleaner (100 W, 42 kHz) for 5 h. After sonication, the powdery Mn_3O_4@rGO nanocomposites were obtained by filtering and vacuum-drying overnight.

Molecular Simulation: Two simulation systems were built in this study. To reduce the simulation cost we reduced the area of graphene nanosheet to 10×10 nm^2 in simulation. In the first step, two 10×10 nm^2 graphene nanosheets were inserted into 15×15×4 nm^3 simulation box. Then the simulation box was filled with THF molecules to model the agglomeration of graphene nanosheets in THF. In the second step, we built the Mn_3O_4 nanocubes/graphene nanosheet in THF solvent system to simulate the assembly of Mn_3O_4 nanocubes on the graphene nanosheet. According to the experimental data, there is one Mn_3O_4 nanocube on 7.07×7.07 nm^2 graphene nanosheet, if the length of the nanocube is 2 nm. Twelve oleylamine chains are grafted onto every facet of the nanocube. The oleylamine modified Mn_3O_4 nanocubes and graphene nanosheet were then solvated in a 15×15×6 nm^3 box filled with THF molecules. The OPLS-AA force field was used for rgraphene, oleylamine and THF molecule.[22] For the Mn_3O_4 nanocubes the non-bonded interaction parameters were from universal force field.[23] The simulation systems were firstly equilibrated for 1 ns at 298 K and 1 atm after energy minimization. Following equilibration, MD simulations were run for a production period of 50 ns in NPT ensemble. The Nosé-Hoover thermostat and barostat were employed to keep the temperature and pressure constant. The van der Waals cutoff radii is 1.2 nm. Long-range electrostatic interaction was calculated using the Particle-Particle and Particle-Mesh (PPPM) method. All the MD simulations were performed by large-scale atomic/molecular massively parallel simulator (LAMMPS).[24]

The orientational order parameter for the backbone of oleylamine is defined as the largest eigenvalue of the Saupe ordering matrix Q:

$$Q = < \frac{3}{2}\cos^2\theta - \frac{1}{2} >$$

where θ is the angle between the bond vector and axis z in this work. <…> is ensemble averaged. The bond vector is the vector between atom i-1 and atom i+1 for atom i.

***Electrochemical Tests*:** Mn_3O_4@rGO hybrid aerogels were compressed and used as anodes directly without binders and current collectors. The mass loading density and areal capacities are based on the weight of Mn_3O_4@rGO hybrid aerogels, other than that of Mn_3O_4. The Mn_3O_4@rGO nanocomposites (powder) were mixed with carbon black and poly(vinylidene fluoride at a weight ratio of 70:15:15, and coated on titanium current collectors to fabricate the anodes. The mass loading density of active materials was about 7 mg cm^{-2}. Half cells were assembled in a glove box with lithium foils as the counter electrode. The 1 M solution of $LiPF_6$ in ethylene carbonate/dimethyl carbonate at a volume ratio of 1:1 was used as the electrolyte. Porous glass fiber membranes were used as the separators.

***Characterizations*:** TEM was performed by a Hitachi HT7700 microscope operated at 100 kV. HRTEM in both TEM and STEM was performed by a FEI Talos F 200X microscope operated at 200 kV. STEM analyses were carried out with a HAADF detector and were accompanied by the high-resolution energy dispersive spectroscopy (EDS) using the SuperX integrated EDS-system with four silicon drift detectors (SDDs). TEM samples are prepared by dispersing the aerogel monolith into ethanol and coating on a copper grid. SEM was performed by a ZEISS LEO 1530 microscope operated at 5 kV. SEM images were taken on the surface and from the core of the aerogel monolith. XPS was performed by a Thermo scientific Sigma 2 spectrometer. XRD was recorded by a PANalytical Empyrean X-ray diffractometer with Cu K_α radiation (λ = 0.154 nm). Raman spectroscopy was recorded by a LabRAM HR Evolution spectrometer (λ = 532 nm). TGA curves were recorded by a Mettler Toledo TGA/SDTA851^e analyzer in air at a heating rate of 10 °C/min. The specific surface area was determined via the Brunauer-Emmett-Teller (BET) method on a Quantachrome Autosorb iQ. Prior to gas sorption analyses with nitrogen at 77 K, the samples were outgassed at 80 °C for at least 18 h. The pore size and pore volume were determined by a density functional theory (DFT) analysis.

Conflicts of interest

There are no conflicts to declare.

Acknowledgements

The authors thank G. Cossu and Prof. A. Rossi for providing the XPS equipment, Prof. J. Vermant for providing TGA equipment, H. Huang for the XPS and TGA measurements, F. Matter for helpful discussions, and the Scientific Center for Optical and Electron Microscopy (ScopeM) of ETH Zürich for access to SEM and TEM facilities. Financial support by ETH Zürich is greatly acknowledged. L.P. acknowledges a fellowship from the Office of China Postdoctoral Council (No. 32 Document of OCPC, 2017). P. Gao and A. M. Tartakovsky acknowledge the funding by the U.S. Department of Energy (DOE) Office of Advanced Scientific Computing Research (ASCR).

Notes and references

1 a) N. Hüsing, U. Schubert, *Angew. Chem. Int. Ed.*, 1998, **37**, 22; b) A. C. Pierre, G. M. Pajonk, *Chem. Rev.*, 2002, **102**, 4243; c) F. Rechberger, M. Niederberger, *Nanoscale Horiz.*, 2017, **2**, 6.

2 a) W. Wei, S. Yang, H. Zhou, I. Lieberwirth, X. Feng, K. Mullen, *Adv. Mater.*, 2013, **25**, 2909; b) H. Long, A. Harley-Trochimczyk, T. Pham, Z. Tang, T. Shi, A. Zettl, C. Carraro, M. A. Worsley, R. Maboudian, *Adv. Funct. Mater.*, 2016, **26**, 5158; c) J. Yu, Q. Li, C.-Y. Xu, N. Chen, Y. Li, H. Liu, L. Zhen, V. P. Dravid, J. Wu, *J. Mater. Chem. A*, 2017, **5**, 3981; d) G. Fu, X. Yan, Y. Chen, L. Xu, D. Sun, J.-M. Lee, Y. Tang, *Adv. Mater.*, 2018, **30**, 1704609.

3 a) F. Rechberger, F. J. Heiligtag, M. J. Sueess, M. Niederberger, *Angew. Chem. Int. Ed.*, 2014, **53**, 6823; b) F. Rechberger, G. Ilari, M. Niederberger, *Chem. Commun.*, 2014, **50**, 13138; c) R. Deshmukh, E. Tervoort, J. Kach, F. Rechberger, M. Niederberger, *Dalton Trans.* 2016, **45**, 11616; d) W. Cheng, F. Rechberger, M. Niederberger, *Nanoscale*, 2016, **8**, 14074; e) W. Cheng, F. Rechberger, M. Niederberger, *ACS Nano*, 2016, **10**, 2467; f) F. Rechberger, M. Niederberger, *Mater. Horiz.*, 2017, **4**, 1115.

4 a) R. Sun, G. Li, W. He, J. Wang, Q. Song, X. Zhang, *Adv. Mater. Interfaces*, 2016, **3**, 1600541; b) W. Chen, S. Qi, L. Guan, C. Liu, S. Cui, C. Shen, L. Mi, *J. Mater. Chem. A*, 2017, **5**, 5332; c) M. A. Garakani, S. Abouali, Z.-L. Xu, J. Huang, J.-Q. Huang, J. K. Kim, *J. Mater. Chem. A*, 2017, **5**, 3547; d) H.-P. Cong, X.-C. Ren, P. Wang, S.-H. Yu, *ACS Nano*, 2012, **6**, 2693; e) S. Parola, B. Julián-López, L. D. Carlos, C. Sanchez, *Adv. Funct. Mater.*, 2016, **26**, 6506.

5 a) H. Zhang, *ACS Nano*, 2015, **9**, 9451; b) C. Lee, X. Wei, J. W. Kysar, J. Hone, *Science*, 2008, **321**, 385.

6 a) S. Han, J. Wang, S. Li, D. Wu, X. Feng, *J. Mater. Chem. A*, 2014, **2**, 6174; b) G. Zeng, N. Shi, M. Hess, X. Chen, W. Cheng, T. Fan, M. Niederberger, *ACS Nano*, 2015, **9**, 4227; c) H. Huang, X. Wang, E. Tervoort, G. Zeng, T. Liu, X. Chen, A. Sologubenko, M. Niederberger, *ACS Nano*, 2018, **12**, 2753; d) X. Liu, T. Ma, L. Sun, Y. Xu, J. Zhang, N. Pinna, *ChemSusChem*, 2018, **11**, 1321; e) R. Wang, S. Wang, D. Jin, Y. Zhang, Y. Cai, J. Ma, L. Zhang, *Energy Storage Mater.*, 2017, **9**, 195; f) X. Wang, S.-X. Zhao, L. Dong, Q.-L. Lu, J. Zhu, C.-W. Nan, *Energy Storage Mater.*, 2017, **6**, 180.

7 a) H. Hu, Z. Zhao, W. Wan, Y. Gogotsi, J. Qiu, *Adv. Mater.*, 2013, **25**, 2219; b) J. Li, J. Li, H. Meng, S. Xie, B. Zhang, L. Li, H. Ma, J. Zhang, M. Yu, *J. Mater. Chem. A*, 2014, **2**, 2934; c) X. Xu, Q. Zhang, Y. Yu, W. Chen, H. Hu, H. Li, *Adv. Mater.*, 2016, **28**, 9223; d) G. Li, G. Hong, D. Dong, W. Song, X. Zhang, *Adv. Mater.*, 2018, **30**, 1801754; e) X. Wu, J. Lyu, G. Hong, X.-c. Liu, X. Zhang, *Langmuir*, 2018, **34**, 9004; f) D. Dong, H. Guo, G. Li, L. Yan, X. Zhang, W. Song, *Nano Energy*, 2017, **39**, 470; g) X. Wang, G. Li, G. Hong, Q. Guo, X. Zhang, *ACS Appl. Mater. Interfaces*, 2017, **9**, 41323; h) G. Li, X. Zhang, J. Wang, J. Fang, *J. Mater. Chem. A*, 2016, **4**, 17042.

8 a) C. Wu, L. Fang, X. Huang, P. Jiang, *ACS Appl. Mater. Interfaces*, 2014, **6**, 21026; b) B. Xie, Y. Zhang, R. Zhang, *J. Mater. Chem. A*, 2017, **5**, 17544.

9 a) K. Chi, Z. Zhang, Q. Lv, C. Xie, J. Xiao, F. Xiao, S. Wang, *ACS Appl. Mater. Interfaces*, 2017, **9**, 6044; b) H. Yin, C. Zhang, F. Liu, Y. Hou, *Adv. Funct. Mater.*, 2014, **24**, 2930; c) L. Li, C. Chen, J. Su, P. Kuang, C. Zhang, Y. Yao, T. Huang, A. Yu, *J. Mater. Chem. A*, 2016, **4**, 10986; d) B. Qiu, M. Xing, J. Zhang, *J. Mater. Chem. A*, 2015, **3**, 12820; e) B. Qiu, Y. Deng, M. Du,

M. Xing, J. Zhang, *Sci. Rep.*, 2016, **6**, 29099; f) B. Qiu, Q. Li, B. Shen, M. Xing, J. Zhang, *Appl. Catal. B-Environ.*, 2016, **183**, 216; g) Q. Zhang, Z. Xu, B. Lu, *Energy Storage Mater.*, 2016, **4**, 84; h) C. Tang, J. Zhu, X. Wei, L. He, K. Zhao, C. Xu, L. Zhou, B. Wang, J. Sheng, L. Mai, *Energy Storage Mater.*, 2017, **7**, 152.

10 a) W. Li, H. Zhang, J. Wang, W. Qiao, L. Ling, D. Long, *Adv. Mater. Interfaces*, 2016, **3**, 1500711; b) I. Andjelkovic, D. N. H. Tran, S. Kabiri, S. Azari, M. Markovic, D. Losic, *ACS Appl. Mater. Interfaces*, 2015, **7**, 9758; c) C. Ba, L. Shi, Z. Wang, G. Chen, S. Wang, Y. Zhao, M. Zhang, S. Yuan, *Res. Chem. Intermed.*, 2017, **43**, 5857; d) J. Lin, S. Yan, P. Liu, X. Chang, L. Yao, H. Lin, D. Lu, S. Han, *Res. Chem. Intermed.*, 2018, **44**, 4503; e) J. Huang, F. Chen, H. Wang, H. Yan, *Res. Chem. Intermed.*, 2018, **44**, 2729.

11 a) J. N. Coleman, *Adv. Funct. Mater.*, 2009, **19**, 3680; Y.-T. Liu, X.-M. Xie, X.-Y. Ye, *Chem. Commun.*, 2013, **49**, 388; c) Y. Hernandez, M. Lotya, D. Rickard, S. D. Bergin, J. N. Coleman, *Langmuir*, 2009, **26**, 3208; d) A. O Neill, U. Khan, P. N. Nirmalraj, J. Boland, J. N. Coleman, *J. Phys. Chem. C*, 2011, **115**, 5422.

12 a) L. Pan, X. D. Zhu, X. M. Xie, Y. T. Liu, *J. Mater. Chem. A*, 2015, **3**, 2726; b) L. Pan, K. X. Wang, X. D. Zhu, X. M. Xie, Y. T. Liu, *J. Mater. Chem. A*, 2015, **3**, 6477; c) L. Pan, X.-D. Zhu, X.-M. Xie, Y.-T. Liu, *Adv. Funct. Mater.*, 2015, **25**, 3341; d) L. Pan, X.-D. Zhu, K.-N. Sun, Y.-T. Liu, X.-M. Xie, X.-Y. Ye, *Nano Energy*, 2016, **30**, 347.

13 S. Bag, K. Roy, C. S. Gopinath, C. R. Raj, *ACS Appl. Mater. Interfaces*, 2014, **6**, 2692.

14 T. Yu, J. Moon, J. Park, Y. I. Park, H. B. Na, B. H. Kim, I. C. Song, W. K. Moon, T. Hyeon, *Chem. Mater.*, 2009, **21**, 2272.

15 a) Y.-T. Liu, Z.-Q. Duan, X.-M. Xie, X.-Y. Ye, *Chem. Commun.*, 2013, **49**, 1642; b) Y.-T. Liu, X.-D. Zhu, Z.-Q. Duan, X.-M. Xie, *Chem. Commun.*, 2013, **49**, 10305; c) L. Pan, Y.-T. Liu, X.-M. Xie, X.-D. Zhu, *Chem. Asian J.*, 2014, **9**, 1519; d) X. Wang, G. Meng, C. Zhu, Z. Huang, Y. Qian, K. Sun, X. Zhu, *Adv. Funct. Mater.*, 2013, **23**, 5771.

16 J. I. Paredes, S. Villar-Rodil, A. Martinez-Alonso, J. M. Tascon, *Langmuir*, 2008, **24**, 10560.

17 a) I. Bilecka, M. Niederberger, *Nanoscale*, 2010, **2**, 1358; b) T. Kim, J. Lee, K.-H. Lee, *Carbon Lett.*, 2014, **15**, 15; c) P. Tang, G. Hu, Y. Gao, W. Li, S. Yao, Z. Liu, D. Ma, *Sci. Rep.*, 2014, **4**, 5901; d) R. Zhang, S. Santangelo, E. Fazio, F. Neri, M. D'Arienzo, F. Morazzoni, Y. Zhang, N. Pinna, P. A. Russo, *Chem. Eur. J.*, *2015*, **21**, 14901; e) N. D. Afify, M. B. Sweatman, *J. Chem. Phys.*, 2018, 148, 024508.

18 a) H. Sun, L. Mei, J. Liang, Z. Zhao, C. Lee, H. Fei, M. Ding, J. Lau, M. Li, C. Wang, X. Xu, G. Hao, B. Papandrea, I. Shakir, B. Dunn, Y. Huang, X. Duan, *Science*, 2017, **356**, 599; b) S. J. Kim, M. Naguib, M. Zhao, C. Zhang, H.-T. Jung, M. W. Barsoum, Y. Gogotsi, *Electrochim. Acta*, 2015, **163**, 246.

19 a) S.-K. Park, A. Jin, S.-H. Yu, J. Ha, B. Jang, S. Bong, S. Woo, Y.-E. Sung, Y. Piao, *Electrochim. Acta*, 2014, **120**, 452; b) M. Jing, J. Wang, H. Hou, Y. Yang, Y. Zhang, C. Pan, J. Chen, Y. Zhu, X. Ji, *J. Mater. Chem. A*, 2015, **3**, 16824; c) J. Tang, W. Liu, H. Wang, A. Gomez, *Adv. Mater.*, 2016, **28**, 10298; d) J.-G. Wang, D. Jin, R. Zhou, X. Li, X.-r. Liu, C. Shen, K. Xie, B. Li, F. Kang, B. Wei, *ACS Nano*, 2016, **10**, 6227; e) J. Yue, X. Gu, L. Chen, N. Wang, X. Jiang, H. Xu, J. Yang, Y. Qian, *J. Mater. Chem. A*, 2014, **2**, 17421; f) X. Gu, J. Yue, L. Li, H. Xue, J. Yang, X. Zhao, *Electrochim. Acta*, 2015, **184**, 250; g) R. Lin, W. Yue, F. Niu, J. Ma, *Electrochim. Acta*, 2016, **205**, 85.

20 a) D. Zhao, Q. Hao, C. Xu, *Electrochim. Acta*, 2015, **180**, 493; b) L. Pan, Y. Liu, X. Xie, X. Ye, X. Zhu, *Nano Res.*, 2016, **9**, 2057; c) B. Liu, L. Qi, J. Ye, J. Wang, C. Xu, *New J. Chem.*, 2017, **41**, 13454; d) D.-J. Yan, X.-D. Zhu, Y.-C. Mao, S.-Y. Qiu, L.-L. Gu, Y.-J. Feng, K.-N. Sun, *J. Mater. Chem. A*, 2017, **5**, 17048; e) R. Zhang, D. Wang, L.-C. Qin, G. Wen, H. Pan, Y. Zhang, N. Tian, Y. Zhou, X. Huang, *J. Mater. Chem. A*, 2017, **5**, 17001.

21 a) J. Polleux, N. Pinna, M. Antonietti, M. Niederberger, *Adv. Mater.*, 2004, **16**, 436; b) F. J. Heiligtag, M. D. Rossell, M. J. Süess, M. Niederberger, *J. Mater. Chem.*, 2011, **21**, 16893.

22 a) W. L. Jorgensen, D. S. Maxwell, J. Tirado-Rives, *J. Am. Chem. Soc.*, 1996, **118**, 11225; b) M. Pykal, P. Jurečka, F. Karlický, M. Otyepka, *Phys. Chem. Chem. Phys.*, 2016, **18**, 6351.

23 A. K. Rappé, C. J. Casewit, K. S. Colwell, W. A. Goddard III, W. M. Skiff, *J. Am. Chem. Soc.*, 1992, **114**, 10024.

24 S. Plimpton, *J. Comput. Phys.*, 1995, **117**, 1.

TABLE OF CONTENT

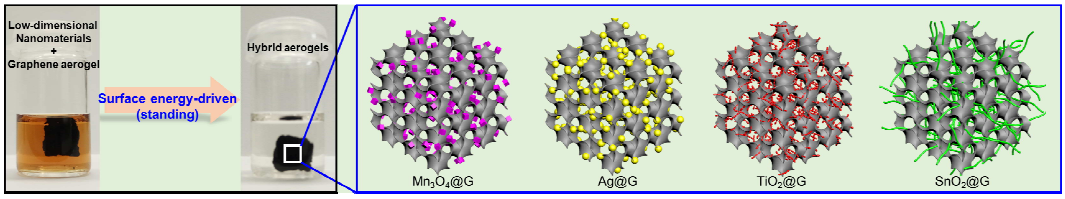

A surface energy-driven strategy is proposed for *ex-situ* hierarchical assembly of low-dimensional nanomaterials on graphene aerogels, which is applicable to a broad variety of low-dimensional nanomaterials regardless of their composition, shapes and dimensionalities. This strategy may open the door towards scalable and straightforward preparation of advanced hybrid aerogels for broad applications in, *e.g.*, energy storage, catalysis, and sensing.

Keyword: surface energy, hierarchical assembly, low-dimensional nanomaterials, graphene, hybrid aerogels, simulation

Surface energy-driven *ex-situ* hierarchical assembly of low-dimensional nanomaterials on graphene aerogels: A versatile strategy

Long Pan,‡[a,*] Peiyuan Gao,‡[b] Elena Tervoort,[a] Alexandre M. Tartakovsky[b] and Markus Niederberger[a,*]